

Direct measurement of the $\bar{K}N \rightarrow \pi\Sigma$ scattering amplitude below the $\bar{K}N$ threshold employing the $d(K^-, N)\pi\Sigma^-$ reaction

Kentaro Inoue

September 25, 2023

Contents

1	Introduction	3
1.1	History of the $\Lambda(1405)$	3
1.2	$\Lambda(1405)$ and the $\bar{K}N$ interaction	4
1.3	J-PARC E31 experiment	5
2	Experimental setup	8
3	Analysis	9
4	Discussion	10
4.1	Template fitting of $K^-d \rightarrow n\pi^+\pi^-n$ events	10
4.1.1	Generated data by Monte Carlo simulation	10
4.1.2	Procedure of template fitting	11
4.1.3	Template fitting of K^0 production reactions	15
4.2	Conversion spectra to cross sections	17
4.2.1	Acceptance correction	17
4.2.2	Conversion spectra to the cross section	19
4.3	Specra	22
4.3.1	Obtained spectra	22
4.3.2	Comparison with theoretical calculations	23
4.3.3	Decomposition of $d(K^-, N)\pi\Sigma$ spectra	25
4.3.4	Fit demonstration for contributions of $I = 0$, $I = 1$, and their interference term	27
5	Conclusion	33
A	Appendix Title.1	35
B	Appendix Title.2	36

Chapter 1

Introduction

In this chapter, we explain our physical motivation, i.e. why $\Lambda(1405)$ is important in the strangeness $S = -1$ sector. We then introduce J-PARC E31 and explain how the reaction mechanism of this experiment provides information on $\bar{K}N \rightarrow \pi Y$ scattering below the $\bar{K}N$ threshold. We explain the advantage of this experiment. We briefly describe obtained spectra and what to discuss in Chapter 4.

1.1 History of the $\Lambda(1405)$

The $\Lambda(1405)$ is a hyperon containing strangeness $S = -1$ with isospin $I = 0$ and spin and spin-parity $J^P = (\frac{1}{2})^-$. In the latest particle data group (PDG) [1], the mass and the width of the $\Lambda(1405)$ are assigned to $1405.1^{+1.3}_{-1.0}\text{MeV}$ and $50.5 \pm 2.0\text{MeV}$ respectively, based on several articles [5, 7, 12].

The existence of the $\Lambda(1405)$ was first predicted by Dalitz and Taun in 1959 as the quasi-bound state of the $\bar{K}N$ [2]. At the Lawrence Radiation Laboratory, a $\Lambda(1405)$ -like excess state was observed in 1961 by the bubble chamber in the $\pi\Sigma$ spectrum using the $K^- p \rightarrow \Sigma\pi\pi\pi$ reaction [3]. They reported a $\Lambda(1405)$ -like excess state in the neutral $\pi\Sigma$ spectrum against to the double charged spectrum, for example $\pi^-\Sigma^-$ or $\pi^+\Sigma^+$ spectra. Hemingway reported the successful high-statistics production of $\Lambda(1405)$ by a hydrogen bubble chamber using a 4.2 GeV K^- beam [4]. They claimed that the identification of the $K^- p \rightarrow \pi\Sigma(1660) \rightarrow \pi\pi\Lambda(1405) \rightarrow \pi\pi(\pi\Sigma)$ reaction lemma enhanced the production of the $\Lambda(1405)$. Dalitz and Deloff applied M-matrix/K-matrix analysis to the $\pi^-\Sigma^+$ spectrum, which is expected to be background-free from non-resonant and $\Lambda(1520)$ in this data, and evaluated the mass and width of $\Lambda(1405)$ at $1406.4 \pm 4.0\text{MeV}$ and $50 \pm 2\text{MeV}$, respectively [5]. This data is employed PDG's estimation for the mass and width of $\Lambda(1405)$.

In the 2000's, the chiral unitary model claimed that the $\Lambda(1405)$ is a dynamical molecular state contributed from two poles, $\pi\Sigma$ in the low-mass

region and $\bar{K}N$ in the high-mass region. According to the this model, the high-mass pole coupled to $\bar{K}N$ is $1426 + 16\text{MeV}$ and the low-mass pole coupled to $\pi\Sigma$ is $1390 + 66i\text{MeV}$. That means the $\pi\Sigma$ spectrum is expected to shift high mass region from the conventional 1405MeV by directly accessing to the $\bar{K}N$ pole.

Experimentally, the $\Lambda(1405)$ production was also carried out employing various reaction mechanisms.

B.Riley et. el. reported $\Sigma^\pm\pi^\mp$ invariant mass of $K^-{}^4\text{He} \rightarrow \pi^\pm\Sigma^\mp$ at rest reaction by stopped K^- using the bubble chamber at Argonne National Laboratory. The analysis by Esmaili et al. based on this experimental results is employed PDG's estimation of the mass of $\Lambda(1405)$ [7].

Niiyama et el. performed photoproduction $\gamma p \rightarrow K^+\Lambda(1405)$ employing a γ beam at $E_\gamma = 1.5 - 2.4\text{GeV}$ at the LEPS beamline in the Spring-8 [8]. They measured the scattering angle in center of mass system of K^+ at $0.8 < \Theta_{K^+} < 1.0$, reported mass spectra of $\pi^-\Sigma^+$ and $\pi^+\Sigma^-$ in the $\Lambda(1405) \rightarrow \pi\Sigma$ decay and observed a difference between the two spectra in the $\Lambda(1405)$ region. This fact means existance of the interference term between the isospin $I = 0$ and $I = 1$ channel. The CLAS collaboration employing a $1.61\text{-}1.91\text{GeV}$ γ beam for photoproduction at the Jefferson Labolatory and measured the scattering angle in center of mass system of K^+ at $0.6 < \Theta_{K^+} < 0.9$ [9, 10]. They reported all three $\pi^-\Sigma^+$, $\pi^+\Sigma^-$ and $\Sigma^0\pi^0$ spectra. The centroid of those three spectra appear to be at 1405MeV , but their lineshapes are different indicating contribution of $I = 1$ strength in this reaction.

The HADES collaboration performed $\Lambda(1405)$ production in p-p collisions using the $3.5\text{GeV}/c$ proton beam [11]. They reported $\pi^-\Sigma^+$, $\pi^+\Sigma^-$ and these average spectra, which clearly show a peak below 1400MeV . The analysis by Hassanvand et al. based on this experimental results is employed PDG's estimation of the mass and the width of $\Lambda(1405)$ [12].

Therefore, the spectrum of $\Lambda(1405)$ depends on the reaction mechanism and the $\pi\Sigma$ charge state for $\Lambda(1405) \rightarrow \pi\Sigma$. This strongly suggests that $\Lambda(1405)$ is a dynamic state, but the mechanism of these reactions is still controversial and its structure is unknown.

1.2 $\Lambda(1405)$ and the $\bar{K}N$ interaction

As mentioned as before section, the $\Lambda(1405)$ has been predicted as a quasi-bound state of the $\bar{K}N$ state and has been discussed as such. In order words, it is necessary the information of the $\bar{K}N$ interaction in order to understand the structure of the $\Lambda(1405)$. In the 1960-70's, various $\bar{K}N$ scattering data from K^- beam were measured with the bubble chamber at the CERN [13–17]. These data were included up to 2.1GeV in the center-of-mass frame and were fitted by partial wave analysis. The KSU group reported the results of

a partial wave analysis using all available $\bar{K}N$ scattering data [18, 19]. The $\bar{K}N$ scattering amplitudes are well analysed, especially in the high energy region. Kamano et. el. developed an improved method, the dynamically coupled channel (DCC) model with two models depending on the treatment of meson-baryon interactions, which was so-called model.A and model.B [20]. A similar picture to the chiral unitary model, where $\Lambda(1405)$ has two poles, was obtained for both models, although the predictions were based on extrapolating the amplitude below the $\bar{K}N$ threshold.

Also, one method of measuring the $\bar{K}N$ scattering length at the $\bar{K}N$ threshold is X-ray from kaonic nuclei. In this method, the X-ray shift emitted by the capture of K^- meson by the nuclei is compared with that of the electromagnetic force alone to assess the effect of the strong force. In 1970-80's, some groups reported $\bar{K}N$ interaction is repulsive by X-ray from the kaonic hydrogen at the CERN, which is inconsistent with the scattering experiment. In 1997, Iwasaki et al. reported this negative shift from a high-resolution experiment at KEK-PS E228 and concluded that the $\bar{K}N$ interaction was an attractive force [21]. This result was verified and updated by the Dear collaboration in 2005 [22] and the SIDDHARTA collaboration in 2011 [23]. The $\bar{K}N$ scattering lengths and effective range obtained by these experiments provide strong constraints on the $\bar{K}N$ scattering amplitude at the $\bar{K}N$ threshold.

Some theoretical groups consistently reproduced the $\bar{K}N$ scattering amplitude on this constraint and scattering data above the $\bar{K}N$ threshold using various approach based on low energy scattering therm [24–28].

1.3 J-PARC E31 experiment

As the situation is described in the previous section, it is desirable to measure $\bar{K}N$ directly scattering amplitudes, especially below the $\bar{K}N$ threshold. However, due to energy conservation laws, kaon and nucleon cannot be directly scattered in free space. Therefore, an experiment using the $d(K^-n)$ reaction was planned and carried out at J-PARC E31 [30]. A similar experiment was carried out at CERN in 1977 using a bubble chamber and reported a spectrum with a peak position shifted to the high mass side above 1405MeV, albeit only in $\Sigma^-\pi^+$ [31]. This spectrum shape was successfully reproduced by theoretical calculations using the chiral unitary model [32]. It is known that P -wave scattering $\Sigma(1385)$ of isospin $I = 1$ exists in the near region. The $\pi\Lambda$ spectrum of $I = 1$ in the same experiment was successfully reproduced by a similar theoretical calculation including P -waves scattering [33]. These theoretical calculations assumed a 2-step reaction, $K^-p \rightarrow KN$ scattering in 1 step and $\bar{K}N \rightarrow \pi\Sigma$ in 2 step.

In this experiment, due to the low momentum of the K^- beam and the unknown angle of the nucleon knocked out in the first step, some argued

that there was a contribution from a reaction in which the K^- beam and nucleon in deuteron were directly converted to $\pi\Sigma$ in the first step reaction and the $\Lambda(1405)$ contribution was unknown.

Therefore, we measured the nucleon knocked out at super-forward angle employing the $d(K^-, n)$ reaction with $1\text{GeV}/c$ K^- beam by the forward detector systems. In the case of a direct reaction between the K^- beam and the nucleon to $\pi\Sigma$, the $\pi\Sigma$ mass is distributed near the kinematic limit ($\sim 1.9\text{GeV}/c$) from the small Fermi momentum of the nucleon in the deuteron and the energy given $\pi\Sigma$ by the K^- beam. This means that the contribution from a direct 1-step reaction is negligible. In the case of 2-step reaction, the $\bar{K}N \rightarrow \pi\Sigma$ scattering of the second step can be accessed to below the $\bar{K}N$ threshold due to the virtual particle of recoiled \bar{K} between the first and second steps. In addition, the momentum transfer is small due to the small momentum of the recoiled \bar{K} , and the second scattering is expected to enhance S -wave scattering against P -wave, D -waves and more higher order wave.

Also, previous experiment reported about $\pi^+\Sigma^-$ and $\pi^-\Lambda$ spectra for $I = 0$ and $I = 1$, respectively. Hence, it was not possible to decompose the isospin for these spectra and discuss the contribution of each isospin, in particular the contribution of the $I = 0$ and $I = 1$ interference term. We identified the final state and decay modes by measuring decay particles from produced hyperons by the cryndrical detectors system surrounding the liquid deuterium target and performed isospin decomposition on the obtained spectra.

Since the J-PARC E31 experiment was proposed, theoretical $\pi\Sigma$ spectra were reported using various $\bar{K}N$ interactions and kinematics. Onishi et al. reported the $\pi^-\Sigma^+$, $\pi^0\Sigma^0$ and $\pi^+\Sigma^-$ spectrum from a full three-body calculation using two types of $\bar{K}N$ interactions, whose one is an effective theory of $\mathbf{SU}(3)$ field, called the energy-dependent model, and the other is a phenomenological potential, called the energy-independent model [34].

Miyagawa et al. reported spectra calculated from two subsystems, $\bar{K}N \rightarrow \bar{K}N$ and $\bar{K}N \rightarrow \pi\Sigma$. The first step $\bar{K}N \rightarrow \bar{K}N$ interaction was used on the basis of recent partial wave analysis [18, 19] as it has a large K^- beam momentum. On the other hand, the second step $\bar{K}N \rightarrow \pi\Sigma$ interaction was used based on various results from the chiral unitary model, a low-energy scattering theory. One is latest chiral unitary analysis by A. Cieplý and J. Smejkal [35] using kaonic hydrogen data from the SIDDAHARTA [23]. Next is the result by Ohnishi et. el. introduced just before [34]. Also, result from earlier chiral unitary analysis by E. Oset, A. Ramos, and C. Bennhold [36] was used.

Kamano et al. also reported predicted spectra for $\pi^-\Sigma^+$, $\pi^0\Sigma^0$ and $\pi^+\Sigma^-$, in addition to $\pi^-\Sigma^0$ as $I = 1$, calculated using the DCC models described before with both model.A and model.B [37].

Our forward detector consists of a forward neutron detector and a for-

ward proton detector and can measure $d(K^-, p)$ in addition to $d(K^-, n)$. In this thesis, we report $\pi^- \Sigma^+$ and $\pi^+ \Sigma^-$ spectra in forward neutron detected events which include scattering amplitude of $I = 0$, $I = 1$ and interference term and $\pi^- \Sigma^0$ spectrum in forward proton detected events which is pure $I = 1$. We performed isospin decomposition to these spectra and obtain pure $I = 0$ spectra and interference term of $I = 0, 1$. We discuss the reaction mechanism from obtained spectra. We discuss the $\Lambda(1405)$ contribution to comparison with $I = 0$ and $I = 1$, and interference term contribution from difference of $\pi^- \Sigma^+$ and $\pi^+ \Sigma^-$ spectra.

Chapter 2

Experimental setup

Chapter 3

Analysis

Chapter 4

Discussion

4.1 Template fitting of $K^-d \rightarrow n\pi^+\pi^-n$ events

4.1.1 Generated data by Monte Carlo simulation

$$K^-d \rightarrow nK^0n \quad (4.1)$$

$$K^-d \rightarrow \pi^\mp\Sigma^\pm n_{missing} \quad (4.2)$$

$$K^-d \rightarrow \pi^\mp\Sigma^\pm n_{forward} \quad (4.3)$$

Since the $K^-d \rightarrow n\pi^+\pi^-n$ event is expected to contain 3 type reactions, (4.1)-(4.3), we obtain the $d(K^-, n)\pi^\mp\Sigma^\pm$ event rejecting K^0 and $\Sigma^\pm_{forward}$ in $K^-d \rightarrow n\pi^+\pi^-n$ event.

We perform template fitting using data reproduced using Monte Carlo simulation (geant4) to decompose into $\pi^-\Sigma^+$ and $\pi^+\Sigma^-$ modes. In this subsection, we explain how we reproduce the data using geant4 simulation.

The K^0 production in (4.1) is simply the so-called quasi-elastic scattering, in which an initial K^- reacts with a proton and is converted into K^0 and a neutron, where the residual neutron is a spectator and its momentum is the Fermi momentum. This reaction causes the scattering angles of the reacting protons and K^- to be distributed in a way that reproduces the past experiment of one nucleon scattering [67], and the momentum of the spectator is also distributed in a way that reproduces the past experiment [69]. In the case of $\Sigma^\pm_{forward}$ production in (4.2), the angular distribution of the past experiment [68] is simulated in the same way.

In the K^0 produced event (4.1), in addition to 1-step reaction described above, events such as a 2-step and direct $\Lambda(1520)$ production are observed. So, we generate data of these reaction. In the case of 2-step reaction, the momentum of recoiled \bar{K} is small and the scattering data of such \bar{K} and nucleon are a few, so the angular distribution and other details are not known. Therefore, the MC data were generated assuming that the scattering of recoiled \bar{K} and nucleons is isotropic. In the case of direct $\Lambda(1520)$

production also no data. Therefore, this data was isotropically scattered $K^-d \rightarrow n\Lambda(1520)$ and $\Lambda(1520)$ decayed to n and K^0 .

Next, we explain the main signal (4.3), which is the backward $\pi\Sigma$ generation. Since there is no data on the invariant mass of $\pi\Sigma$, it is generated as a uniform distribution from the $\bar{K}N$ threshold, whose lineshape is determined by template fitting. There is also no data on the scattering angle of $\pi\Sigma$, but since the $\bar{K}N \rightarrow \pi\Sigma$ scattering is expected to be S -wave in this reaction, we assume that it is isotropic and generate MC data.

In summary, the following seven MC data are used for template fitting.

- About K^0 production reaction

- $K^-d \rightarrow n_{forward}K^0n_{spectator}$ (K^0 1-step)
- $K^-d \rightarrow n_{forward}(K^0n)_{isotropic}$ (K^0 2-step)
- $K^-d \rightarrow n\Lambda(1520) \rightarrow nK^0n$ (direct $\Lambda(1520)$)

- About $\Sigma_{forward}$ production reaction

- $K^-d \rightarrow \Sigma^+\pi^-n_{spectator} \rightarrow n_{forward}\pi^+\pi^-n_{spectator}$ (Σ^+ 1-step)
- $K^-d \rightarrow \Sigma^-\pi^+n_{spectator} \rightarrow n_{forward}\pi^-\pi^+n_{spectator}$ (Σ^- 1-step)

- About backward $\pi\Sigma$ production reaction

- $K^-d \rightarrow n_{forward}\pi^-\Sigma^+$ (backward $\pi^-\Sigma^+$)
- $K^-d \rightarrow n_{forward}\pi^+\Sigma^-$ (backward $\pi^+\Sigma^-$)

4.1.2 Procedure of template fitting

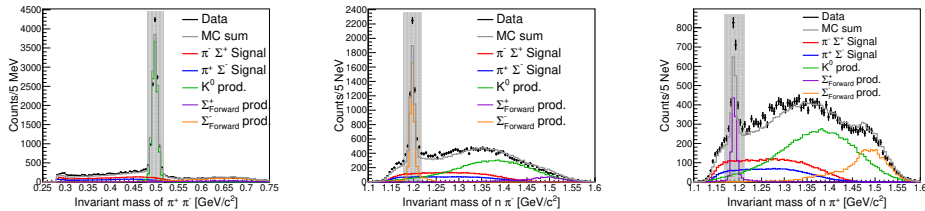


Figure 4.1: The figures show template fitting for background estimation. The right, center, and left figures show invariant masses of $\pi^+\pi^-$, $n\pi^-$ and $n\pi^+$, respectively. Error bars indicate data spectra. Bold lines indicate backward $\pi\Sigma$ production signals, red and blue indicate $\pi^-\Sigma^+$ and $\pi^+\Sigma^-$, respectively. The green, purple, and orange thin lines indicate the K^0 , $\Sigma^-_{forward}$ and $\Sigma^+_{forward}$ production reactions. Gray lines indicate the sum of MC simulations. Gray hatching indicates the 3σ rejection region estimated by fitting with Gaussian and polynomial backgrounds.

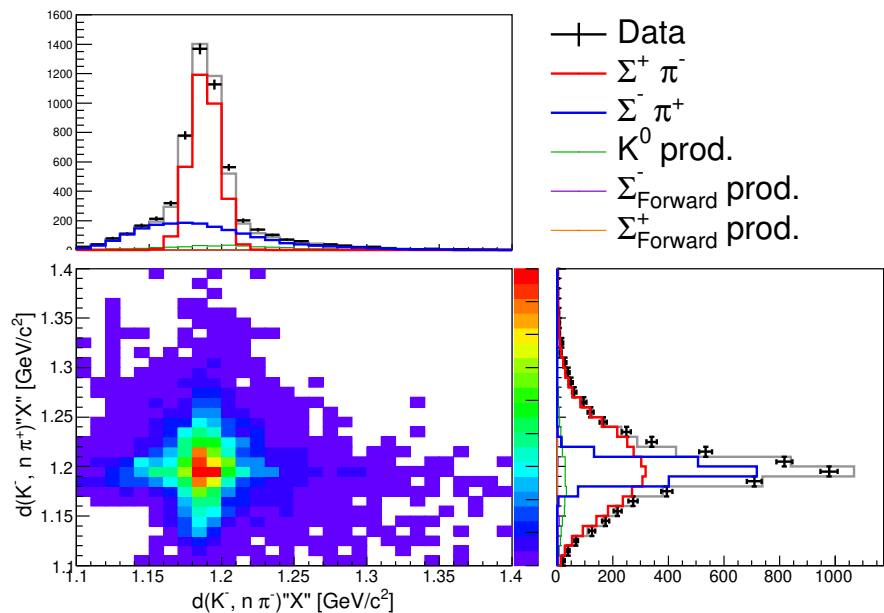


Figure 4.2: This figure shows template fitting of the $d(K^-, n\pi)$ spectra to separate the $\pi^- \Sigma^+$ and $\pi^+ \Sigma^-$ modes. The down left figure shows two-dimensional plots of $d(K^-, n\pi^-)$ and $d(K^-, n\pi^+)$ on the horizontal and vertical axes, respectively. The top and right figures show the projection of each axis. The caption is same as Figure 4.1.

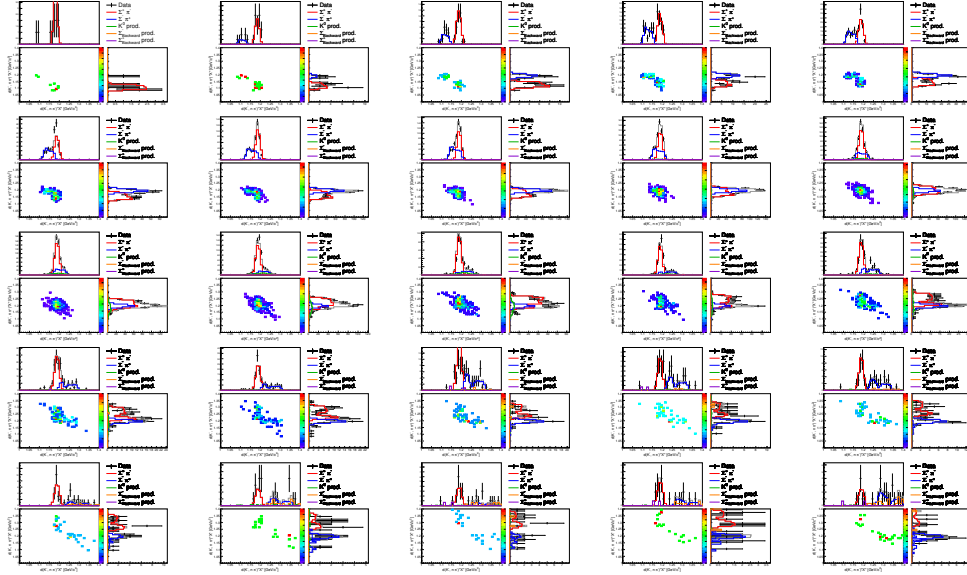


Figure 4.3: These figures are presented separately for each bin of $d(K^-, n)$ for fitting to separate $\pi^-\Sigma^+$ and $\pi^+\Sigma^-$ modes. The top left figure shows the lowest missing mass in the 1.35-1.36GeV bin, with the next bin represented as one goes to the right. In other words, one row is shown for the 0.05GeV region.

In this subsection, we explain procedure of template fitting, whose main purpose is decomposition of $\pi^-\Sigma^+$ and $\pi^+\Sigma^-$ modes. Template fitting is divided into two stages, one fitting to estimate the amount of background for K^0 and $\Sigma_{forward}$ production, the other to separate $\pi^-\Sigma^+$ and $\pi^+\Sigma^-$ modes. These fittings are performed using fitting with the likelihood method on a finite sample generated by Monte Carlo method [71]. There is no χ^2 in this fitting, but there is a value of $-2 \log \Lambda$ that asymptotically approaches the χ^2 when the number of samples become infinite, and the fitting is evaluated with this value. Here, Λ is the likelihood.

The first fitting is performed using the invariant mass distributions of $\pi^+\pi^-$, $n\pi^+$ and $n\pi^-$ in the event that $K^-d \rightarrow n\pi^+\pi^-n$ final state. The K^0 , Σ^+ and Σ^- productions create peaks in the respective invariant mass distributions as shown in Fig.4.1. The distributions reconstructed by fitting are also plotted in the same figure. The bold line represents the case of backward $\pi\Sigma$ production of signal, with red and blue representing the $\pi^-\Sigma^+$ and $\pi^-\Sigma^+$ modes, respectively. The other green, purple and orange lines represent the background for K^0 , $\Sigma_{forward}^-$ and $\Sigma_{forward}^+$ production, respectively. This fitting of $-2 \log \Lambda$ is 1077.4. Degrees freedom is the number of bin with data, and $-2 \log \Lambda/NDF \sim 3.06$.

The fitting to separate the $\pi^-\Sigma^+$ and $\pi^+\Sigma^-$ modes is performed for

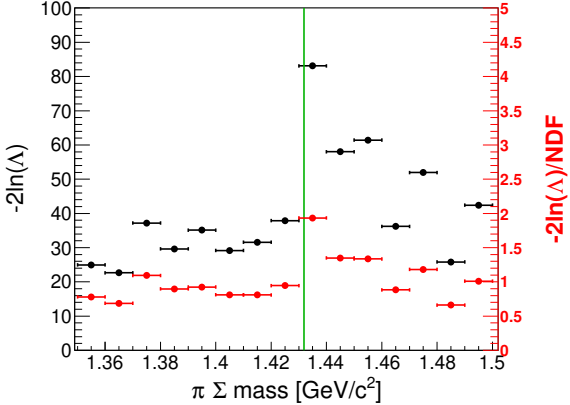


Figure 4.4: This figure shows the template fitting $-2 \log \Lambda$ and $-2 \log \Lambda/NDF$ for the separation of $\pi^-\Sigma^+$ and $\pi^+\Sigma^-$ modes in each $d(K^-, n)$ bin. Black and red indicate $-2 \log \Lambda$ and $-2 \log \Lambda/NDF$, respectively. The horizontal axis is represented for $d(K^-, n)$ bins.

events from $K^- - d \rightarrow n\pi^+ \pi^- - n$, excluding K^0 and $\Sigma_{forward}^\pm$ production. However, the background leakage is estimated by scaling the distribution reconstructed in the MC simulation by the intensity estimated by the invariant mass fitting. This fitting is performed each bin of the missing mass of $d(K^-, n)$, since the scattering amplitude of $\bar{K}N \rightarrow \pi\Sigma$ depends on the $\pi\Sigma$ invariant mass. For this fitting we use the $d(K^-, n\pi^-)$ and $d(K^-, n\pi^+)$ missing masses as shown in Fig.4.2. This figure shows the sum of the $d(K^-, n)$ bins. The bottom left figure shows a two-dimensional figure of the $d(K^-, n\pi^-)$ and $d(K^-, n\pi^+)$ missing masses on the horizontal and vertical axes, respectively. The top and right figures show the projections of the respective axes. The missing mass of $d(K^-, n\pi)$ makes a peak at Σ for the correct combination for the missing Σ , but is widely distributed in the kinematic region for the opposite charge. For example, for $d(K^-, n\pi^-)$, the $\pi^-\Sigma^+$ mode has a peak structure as shown by the red line, whereas the $\pi^+\Sigma^-$ mode has a widely distributed structure as shown by the blue line.

Fig.4.1.2 shows the results for the fitting of each bin of $d(K^-, n)$ separately. Fig.4.4 shows the $-2 \log \Lambda$ and $-2 \log \Lambda/NDF$ of this fitting in each $d(K^-, n)$ bin in black and red, respectively.

Fitting to estimate background and to separate $\pi^-\Sigma^+$ and $\pi^+\Sigma^-$ modes cannot be performed simultaneously as they use different event samples. They are therefore repeated in the following steps.

First, the separation of $\pi^-\Sigma^+$ and $\pi^+\Sigma^-$ modes is performed without considering the background. The obtained distribution of backward $\pi^\mp\Sigma^\pm$ modes is used for fitting to estimate the background, which is then fed back into the fitting of the separation of $\pi^-\Sigma^+$ and $\pi^+\Sigma^-$ modes. After five iterations of this procedure, fitting is performed considering 2-step and

direct $\Lambda(1520)$ generation for K^0 generation, which is described in the next subsection. Finally, fitting of the separation of the $\pi^-\Sigma^+$ and $\pi^+\Sigma^-$ modes is performed to obtain the final $\pi\Sigma$ spectrum as shown in Fig.4.5..

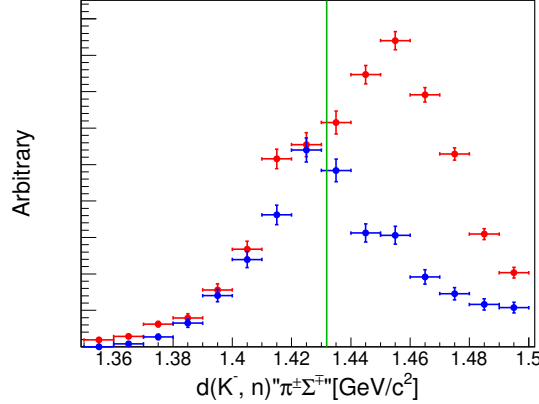


Figure 4.5: The $\pi^-\Sigma^+$ and $\pi^+\Sigma^-$ mode spectra with arbitrary scale by template fitting are shown. Red and blue lines indicate $\pi^-\Sigma^+$ and $\pi^+\Sigma^-$, respectively. Green vertical line is indicated the $\bar{K}N$ threshold.

4.1.3 Template fitting of K^0 production reactions

In this subsection, we explain about template fitting for K^0 production reactions and these reactions. Template fitting to decompose the K^0 production reactions is preformed by means of Figure.4.6, which shows the nK^0 invariant masses of the events identified with K^0 from the final state of $K^-d \rightarrow n\pi^+\pi^-n$.

In 1-step reaction, the missing neutrons are spectator and have small momentum, so the nK^0 invariant mass should be concentrated near the kinematic limit. However, the data between the $\bar{K}N$ threshold and the kinematic limit contain a broadly distributed component is observed, as shown in Figure.4.6. This component is thought to be the recoiled \bar{K} scattering with the residual nucleon and sharing its momentum. Actually, this component can be reproduced by data generated by MC simulations assuming 2-step reaction. A bump structure is observed near $\Lambda(1520)$, indicating that $K^-d \rightarrow n\Lambda(1520)$ reaction and $\Lambda(1520) \rightarrow nK^0$ decay are taking place. As a result of this template fit, the $-2 \log \Lambda$ is estimates as 275.2 and NDF is 43, so $-2 \log \Lambda/NDF \sim 6.40$. The, the ratio of 1-step to true K^0 production excluding background is estimated to $80.9 \pm 1.3\%$, 2-step $11.5 \pm 1.0\%$ and direct- $\Lambda(1520)$ $7.7 \pm 0.6\%$.

We explain effect of these reactions contaminating into the main signal as background. Since the spectral shape of $d(K^-, n)$ is determined by the initial $\bar{K}N$ scattering, the 2-step reaction is almost identical to the 1-step

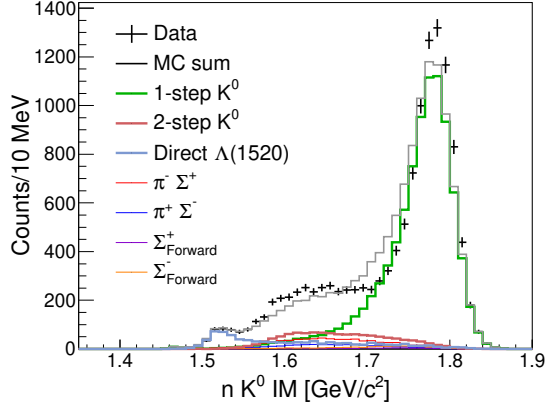


Figure 4.6: The figure shows nK^0 invariant masses and template fitting for the reaction decomposition of K^0 production events. Error bars indicate data. Bold lines indicate MC sim for 1-step K^0 , 2-step K^0 , and direct $\Lambda(1520)$ production reactions in green, dark red, and dark blue, respectively. Thin lines indicate background events in K^0 production reactions, backward $\pi^-\Sigma^+$, backward $\pi^+\Sigma^-$, $\Sigma_{forward}^+$, and Σ^- in red, blue, purple, and orange.

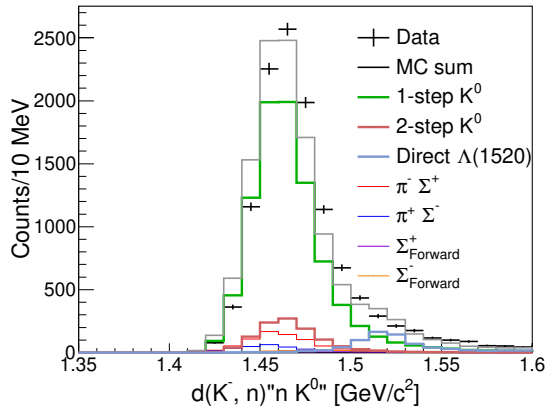


Figure 4.7: This figure shows the $d(K^-, n)$ missing mass due to K^0 tagging events. Contamination to the backward $\pi^\mp\Sigma^\pm$ signal is estimated based on this spectrum. The caption is the same as in Figure 4.6..

reaction. On the other hand, the direct $\Lambda(1520)$ production makes a bump structure on $d(K^-, n)$ too. Since the contribution of this reaction is so small, this background effect is almost no change.

4.2 Conversion spectra to cross sections

4.2.1 Acceptance correction

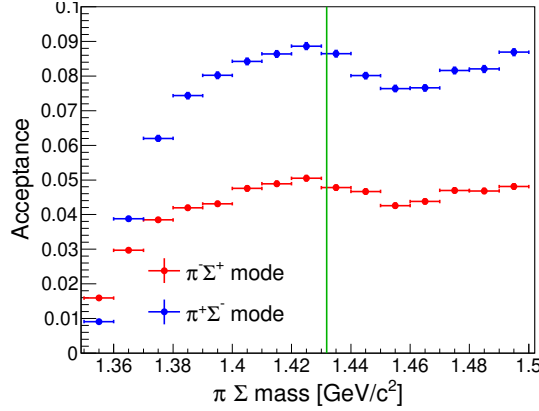


Figure 4.8: This figure shows the acceptance of $d(K^-, n)\pi^\mp\Sigma^\pm$. The red line indicates $\pi^-\Sigma^+$ and the blue line indicates $\pi^+\Sigma^-$.

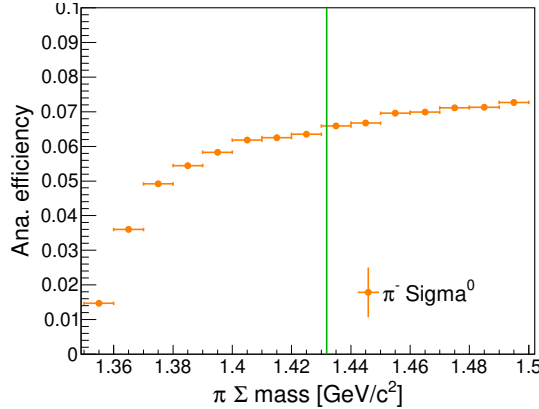


Figure 4.9: This figure shows $d(K^-, p)\pi^-\Sigma^0$ acceptance

The acceptance of $d(K^-, n)\pi^\mp\Sigma^\pm$ and $d(K^-, p)\pi^-\Sigma^0$ is corrected by MC simulations in which nucleons are injected at a forward angle into the covered region of a forward detector with a uniform $\pi\Sigma$ mass distribution. Since the solid angle of the forward detector is evaluated as subsection.??, we adapt as the denominator the events for which the forward detector is

analyzable. The same analysis procedure as for the real data is applied to the MC simulation, and the final survival rate is evaluated and used as the acceptance. That is, for $d(K^-, n)\pi^\mp\Sigma^\pm$, we apply $d(K^-, n\pi^+\pi^-)n$ final state selection and rejection of K^0 and $\Sigma_{forward}$. For $d(K^-, p)\pi^-\Sigma^0$, we apply the $d(K^-, p\pi^-\pi^-)p\gamma$ and $d(K^-, p\pi^-)\Sigma^0$ selections. Fig.4.8 shows the acceptance of $d(K^-, n)\pi^\mp\Sigma^\pm$. Dents above the $\bar{K}N$ threshold are due to K^0 rejection. The difference in absolute values between $\pi^-\Sigma^+$ and $\pi^+\Sigma^-$ is due to the branching ratio of the Σ decay. Fig.4.9 shows the acceptance of $d(K^-, p)\pi^-\Sigma^0$.

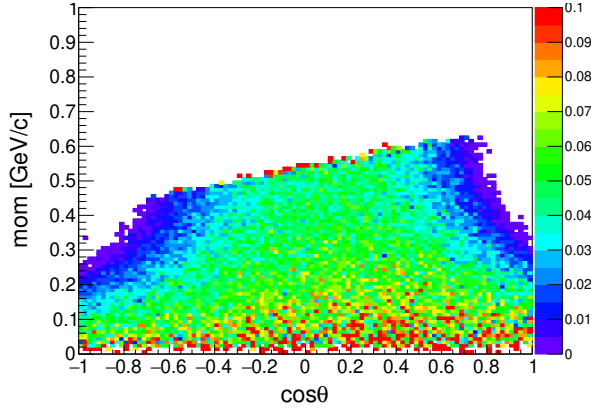


Figure 4.10: This figure shows the 2D acceptance map for $d(K^-, n)nK^0$. The horizontal axis shows the scattering angle of K^0 in the Lab. frame, and the vertical axis shows the momentum of K^0 .

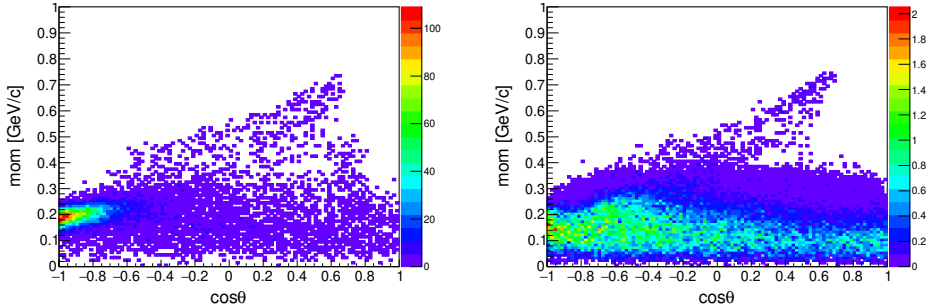


Figure 4.11: These figure shows scattering angle and momentum of K^0 . The right and left figure indicate data and background. The background is reproduced from MC simulations.

For K^0 production events, we use acceptance for K^0 kinematics because all detected particles are of K^0 origin. We estimate the two-dimensional acceptances for K^0 momentum and K^0 scattering angles as shown in Fig.??, and weight each event to correct for acceptances. Fig.4.12 shows acceptance

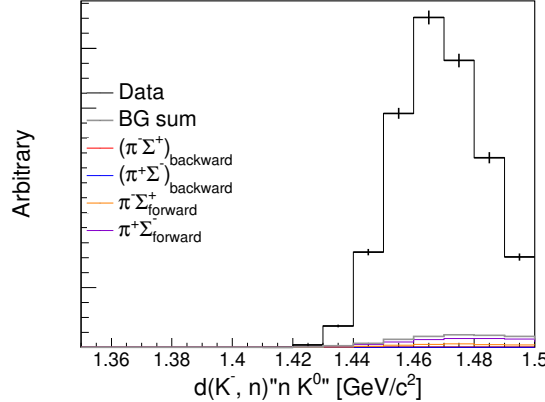


Figure 4.12: This figure shows the $d(K^-, n)''n K^0''$ corrected acceptance with caption is the same as in Figure.4.7.

corrected spectra of K^0 production with reproduced BG by MC simulations. It can be seen that the data are concentrated in the backward and high momentum regions where the acceptances are small, while the MC is distributed over the whole region as shown in Fig.4.11. In other words, the acceptance correction suppresses BG and emphasizes true K^0 production.

4.2.2 Conversion spectra to the cross section

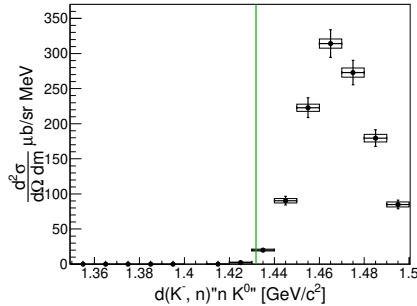


Figure 4.13: This figure shows the cross section of $d(K^-, n)''n K^0''$. The box represents the statistical error, and the error bar represents the root mean squares of the conversion factor added to it. The green vertical lines indicates $\bar{K}N$ threshold.

The obtained spectra are converted to cross sections. For this purpose, the target, beam, and DAQ efficiencies are summarized as luminosity. The target and beam quantities are discussed in Sections.?? and ??, respectively. The DAQ efficiency consists of two parts, one of which is the DAQ live rate and the other is the trigger efficiency, described in Sections.?? and ??.

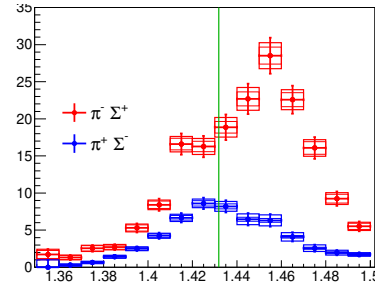


Figure 4.14: The red figure and blue figure shows about $d(K^-, n)\pi^+\Sigma^-$ and $d(K^-, n)\pi^-\Sigma^+$, respectively. The inner frame (thin line), outer frame (thick line), and error bars represent the addition of statistical errors, fitting errors, and conversion errors, which were calculated by root-mean-square. The green vertical lines indicates $\bar{K}N$ threshold.

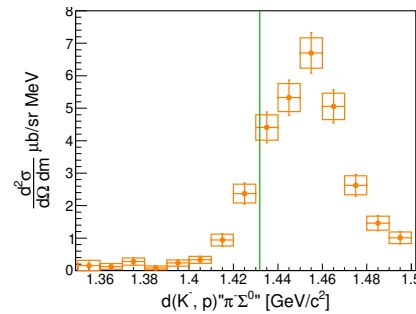


Figure 4.15: This figure shows the cross section of $d(K^-, p)\pi^-\Sigma^0$. The box represents the statistical error, and the error bar represents the root mean squares of the conversion factor added to it. The green vertical lines indicates $\bar{K}N$ threshold.

Table 4.1: Summary table of $d(K^-, n)$ scaling parameters

Component	value	error	value	error
Luminosity ($/\mu b$)	5927	158		
Target Length (cm)			10	
Target density [g/cm^3]			$0.1613 - 0.1617$	0.0015
Number of Kaon			5.83×10^{10}	
Survival ratio of K^-			0.281	0.0003
DAQ live ratio			0.768	0.0021
Trigger efficiency				
$K \otimes CDH1$			0.9527	0.0004
Neutral			0.9992	6.7×10^{-6}
Efficiency of the CDC	0.977	0.04		
Efficiency of the NC	0.291	0.015		
Intrinsic the NC			0.317	0.016
Over veto of the CVC/BVC			0.081	0.007

Table 4.2: Summary table of $d(K^-, p)$ scaling parameters

Component	value	error	value	error
Luminosity ($/\mu b$)	2478	81		
Target Length (cm)			10	
Target density [g/cm^3]			0.1624	0.0014
Number of Kaon			2.05×10^{10}	
Survival ratio of K^-			0.336	0.0001
DAQ live ratio			0.821	0.0001
Trigger efficiency				
$K \otimes CDH1$			0.9527	0.0003
Charge			0.9559	0.0004
Efficiency of the CDC	0.977	0.04		
Efficiency of the forward detectors	0.819	0.042		

Detector efficiency is also evaluated and corrected for conversion to cross sections. The CDC, NC, and PC efficiencies are described in Sections.??, ??, and ??, respectively. These conversion factors are common for the $\pi\Sigma$ spectra. These factors are summarized in Table.4.1 and Table.4.2 about $d(K^-, n)$ and $d(K^-, p)$, respectively.

On the other hand, the acceptances depend on the $\pi\Sigma$ mass spectra. In the case of $d(K^-, n)\pi^\mp\Sigma^\pm$, the separation ratio of $\pi^-\Sigma^+$ and $\pi^+\Sigma^-$ is also depend on. We obtain the cross section of $d(K^-, n)nK^0$, $d(K^-, n)\pi^-\Sigma^0$ and $d(K^-, p)\pi^-\Sigma^0$ by adapting the these corrections, which are shown in Figure.4.13, Figure.4.14, and Figure.4.15, respectively.

4.3 Spectra

4.3.1 Obtained spectra

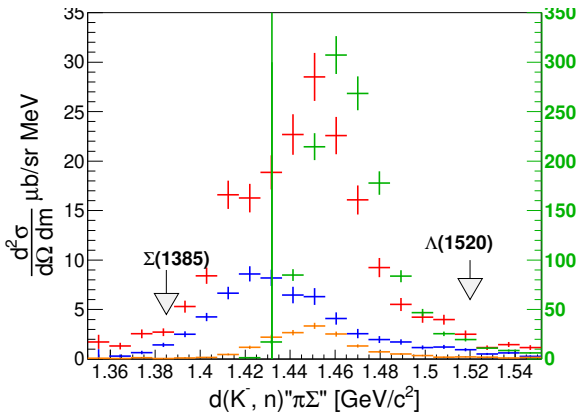


Figure 4.16: The obtained cross sections are plotted simultaneously in this figure. The $d(K^-, n)\pi^-\Sigma^+$, $d(K^-, n)\pi^+\Sigma^-$, $d(K^-, n)nK^0$, and $d(K^-, p)\pi^-\Sigma^0$ plot as red, blue, green, and orange, lines respectively. The $d(K^-, n)nK^0$ is scaled to 1/10. The green virtual line indicates the $\bar{K}N$ threshold.

In this subsection we discuss the physical meaning of the obtained spectra, for which we simultaneously plot the obtained spectra in Figure.4.16. In this figure, $d(K^-, n)nK^0$ is scaled to 1/10 for comparison with 1-step quasi-elastic scattering.

The $d(K^-, n)nK^0$ spectra do not contain information below the $\bar{K}N$ threshold but are suitable for studying the $d(K^-, n)$ reaction. This spectrum is similar to the bump structure of the so-called quasi-elastic scattering. This spectrum contains about 12% of the 2-step reaction described in the previous section. Since the missing mass of $d(K^-, n)$ is determined by the $K^-N \rightarrow \bar{K}N$ scattering of the first reaction, this spectrum has almost the

same shape as quasi-elastic scattering. The strength of the 2-step at the quasi-elastic scattering bump is $35mb/\Omega \cdot \text{MeV}$, which is consistent with $d(K^-, N)\pi\Sigma$ in order.

Next, we discuss the $d(K^-, N)\pi\Sigma$ including the scattering amplitude below the $\bar{K}N$ threshold. There is an $I = 1$ p-wave state, $\Sigma(1385)$, and an $I = 0$ d-wave state, $\Lambda(1520)$, near the $\bar{K}N$ threshold. However, the pure $I = 1$ $d(K^-, p)\pi^-\Sigma^0$ spectrum has no structure around the region of $\Sigma(1385)$, and the $d(K^-, n)\pi^\mp\Sigma^\pm$ spectrum contributed from $I = 0$ and $I = 1$ has no structure around $\Sigma(1385)$ and $\Lambda(1520)$. This means that in the $d(K^-, N)\pi\Sigma$ reaction, the P -wave, D -wave, and higher-order waves are suppressed and the S -wave is dominant.

The $d(K^-, p)\pi^-\Sigma^0$ spectrum resembles the bump structure of quasi-elastic scattering. In other words, the spectrum strongly reflects the first $K^-N \rightarrow \bar{K}N$ scattering because there is no pole near the $\bar{K}N$ threshold and there is no significant change in the amplitude of the second $\bar{K}N \rightarrow \pi\Sigma$ scattering at $I = 1$.

On the other hand, an excess strength below the $\bar{K}N$ threshold is observed in the $d(K^-, n)\pi^\mp\Sigma^\pm$ spectrum, which is considered to be a contribution from the $I = 0$ amplitude of second $\bar{K}N \rightarrow \pi\Sigma$ scattering. The $I = 0$ and $I = 1$ interference terms at the second $\bar{K}N \rightarrow \pi\Sigma$ scattering amplitude appears as the difference between the $\pi^-\Sigma^+$ and $\pi^+\Sigma^-$ spectra. This difference is observed in the obtained $d(K^-, n)\pi^\mp\Sigma^\pm$ spectrum, whose behavior changes dramatically above and below the $\bar{K}N$ threshold. The scattering amplitude changes dramatically at the poles. This effect is emphasized by the scattering particle mass threshold. Thus, the observed interference term suggests that the pole exists just below the $\bar{K}N$ threshold.

4.3.2 Comparison with theoretical calculations

The qualitative property of obtained spectra is discussed in the previous subsection. In this subsection, we discuss the more detail quantitative property by comparing to expected spectra of theoretical calculations. These theoretical calculations are based on 2-step reaction as described in chapter.1. This validity is confirmed in previous subsection.

In the present reaction, the first and second scattering have different kinetic regions. The first scattering is in the high-energy region with a total energy of 2.05 GeV, and the $\bar{K}N$ scattering data are abundant in this region and its scattering amplitude is determined with good accuracy. On the other hand, the second scattering is in the low energy region around the $\bar{K}N$ threshold, and the $\bar{K}N$ scattering data in this region are not sufficient, especially the scattering amplitude below the $\bar{K}N$ threshold cannot be measured by the elementary process. One is a method in which the first scattering is calculated using partial wave analysis and the second scattering is calculated using the results of a low-energy coupled-channels analysis

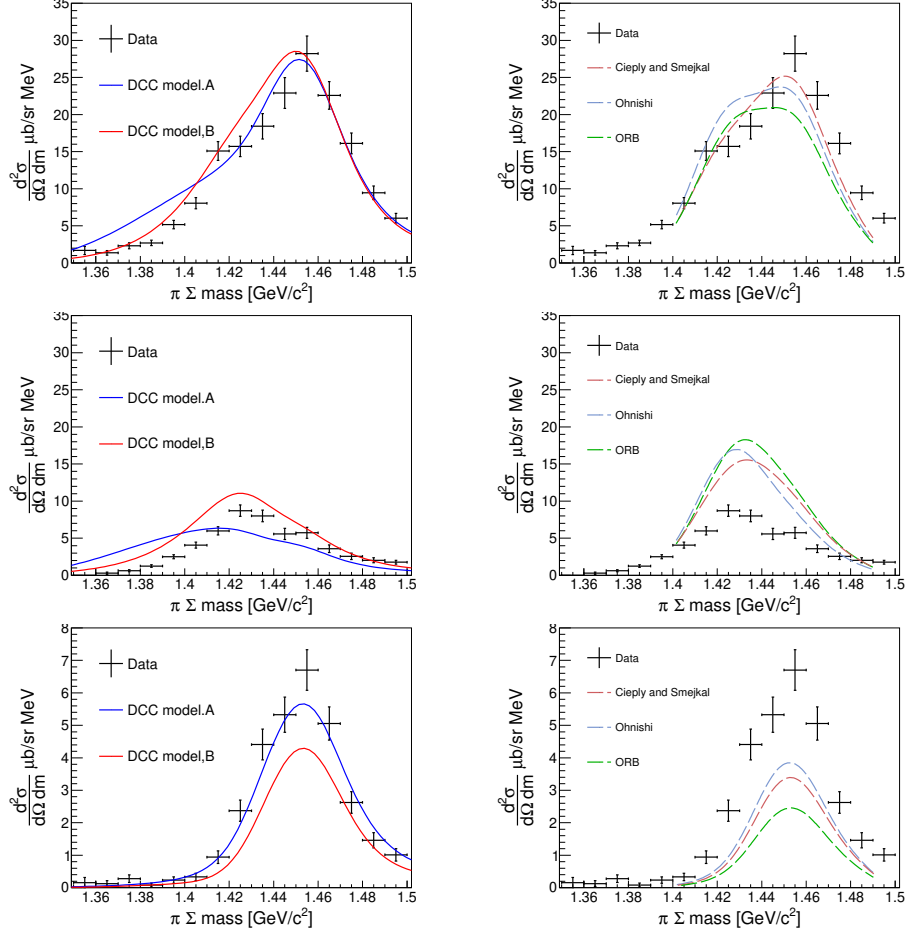


Figure 4.17: This figure shows a comparison of our obtained spectra with predictions from theoretical calculations. The top, middle, and bottom figures represent $\pi^- \Sigma^+$, $\pi^+ \Sigma^-$, and $\pi^- \Sigma^0$, respectively. The right figure shows the spectrum predicted by the DCC model, and the left figure shows the spectrum predicted by the calculation of Miyagawa et al. The spectra predicted by theoretical calculations are convoluted with our detector resolution.

of the $\bar{K}N$ interaction. One is a method in which the first scattering is calculated using the recent partial wave analysis and the second scattering is calculated using the results of a 3 different low-energy coupled-channels analysis of the $\bar{K}N$ interaction. The second one is based on the so-called DCC model, which determines the $\bar{K}N \rightarrow$ meson-baryon scattering amplitudes from various $\bar{K}N \rightarrow$ meson-baryon scattering data in wide momentum region with meson-baryon interactions based on coupled-channel methods. Figure.4.17 compares the obtained spectra with the theoretical predictions convolved with the experimental resolution. The upper, middle, and lower panels are shown for $\pi^-\Sigma^+$, $\pi^+\Sigma^-$, and $\pi^0\Sigma^-$, respectively. The right and left panels show the predictions by the DCC model and the calculations by Miyagawa et al.

The predictions of the DDC model explain the cross sections well for all spectra, whereas the predictions of Miyagawa et al. cannot explain the obtained spectra due to the lack of overall strength at $\pi^0\Sigma^-$ and the excess of overall strength at $\pi^+\Sigma^-$. Therefore, in the following, we discuss $I = 0$ and $I = 1$ and their interference in more detail based on the DCC model.

4.3.3 Decomposition of $d(K^-, N)\pi\Sigma$ spectra

In this subsection, we decompose the obtained spectra into $I = 0$, $I = 1$ and their interference terms, and discuss how each of them affects the spectrum. Based on the two-step reaction mechanism described so far, the obtained $d(K^-, N)\pi\Sigma$ spectrum can be expressed as follows.

$$\begin{aligned} \frac{d\sigma}{d\Omega dM}(\pi^\mp\Sigma^\pm) &\propto |C_{K^-N \rightarrow \bar{K}N}^0 T_{\bar{K}N \rightarrow \pi\Sigma}^{I=0} \mp C_{K^-N \rightarrow \bar{K}N}^1 T_{\bar{K}N \rightarrow \pi\Sigma}^{I=1}|^2 \\ &= |C_{K^-N \rightarrow \bar{K}N}^0 T_{\bar{K}N \rightarrow \pi\Sigma}^{I=0}|^2 + |C_{K^-N \rightarrow \bar{K}N}^1 T_{\bar{K}N \rightarrow \pi\Sigma}^{I=1}|^2 \\ &\mp 2\text{Re}(C_{K^-N \rightarrow \bar{K}N}^0 C_{K^-N \rightarrow \bar{K}N}^1 T_{\bar{K}N \rightarrow \pi\Sigma}^{I=0} T_{\bar{K}N \rightarrow \pi\Sigma}^{I=1}) \end{aligned} \quad (4.4)$$

$$\frac{d\sigma}{d\Omega dM}(\pi^-\Sigma^0) \propto |C_{K^-N \rightarrow \bar{K}N}^1 T_{\bar{K}N \rightarrow \pi\Sigma}^{I=1}|^2 \quad (4.5)$$

Here, $T_{\bar{K}N \rightarrow \pi\Sigma}^{I=0,1}$ is T matrix of second $\bar{K}N \rightarrow \pi\Sigma$ scattering with $I = 0, 1$. And, $C_{K^-N \rightarrow \bar{K}N}^{0,1}$ represent the factor of first $K^-p \rightarrow \bar{K}N$ scattering about $I = 0, 1$ of the second scattering. These are complex values that depend on the total energy of the scattering and are $\pi\Sigma$ invariant mass in the case of the second scattering.

Figure.4.18 shows the decomposition into $I = 0$, $I = 1$, and their interference terms according to Eq.(4.4, 4.5). For comparison, the same procedure for the spectra predicted from the DCC model is also plotted.

These are discussed in turn. First, the interference term are in good agreement with our experimental values for both Model.A and Model.B.

Second, for $I = 1$, the spectral shape strongly reflects the quasi-elastic scattering, which is consistent with both Model.A and Model.B. However,

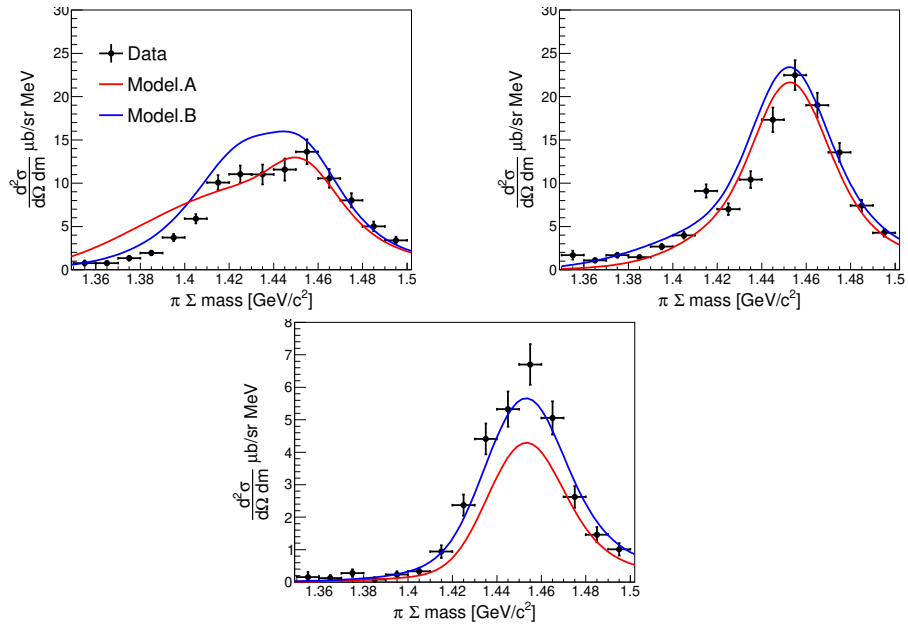


Figure 4.18: These figures show a comparison between our data and theoretical calculations of the DCC models (models.A and model.B). The black error bars represent our data. The blue and red lines represent Model.A and Model.B respectively. The top right figure shows the strength of $I = 0$, the top left figure shows the interference term and the bottom figure shows the strength of $I = 1$.

Table 4.3: This table shows the pole position with $I = 0$ and $J^P = 1/2^-$ below the $\bar{K}N$ threshold by DCC models [37]

	pole1	pole2
Model.A	$1437 - 75i$	$1372 - 56i$
Model.B	$1428 - 31i$	$1397 - 98i$

the strength of Model.A is less than our experimental data.

Next, consider the $I = 0$ channel, which reflects the effect of $\Lambda(1405)$. For Model.A, the spectral shape seems to reproduce our experimental data well, although the overall strength is somewhat larger. On the other hand, Model.B has a long tail below the $\bar{K}N$ threshold and this part does not match the spectral shape of our experiment.

Model .A has a large width at the higher pole that is strongly reflected in this response as shown in Table.4.3, thus Model.A has a large tail component below the $\bar{K}N$ threshold.

In the next subsection, we discuss how these components affect the spectra by parameterizing them by the scaling factor of each component of the DCC model.

4.3.4 Fit demonstration for contributions of $I = 0$, $I = 1$, and their interference term

First, free parameterize the strength of the second scattering of isospin $I = 0, 1$ as $T_{\bar{K}N \rightarrow \pi\Sigma}^{I=0,1} = A_{I=0,1} T_{\bar{K}N \rightarrow \pi\Sigma}^{I=0,1}$, where $A_{I=0,1}$ is the free parameters.

Here, the scattering strength of $I = 1, 0$ and its interference term are expressed as

$$f_{I=0}(m_{\pi\Sigma}) = |C_{K^-N \rightarrow \bar{K}N}^0 T_{\bar{K}N \rightarrow \pi\Sigma}^{I=0}|^2 \quad (4.6)$$

$$f_{I=1}(m_{\pi\Sigma}) = |C_{K^-N \rightarrow \bar{K}N}^1 T_{\bar{K}N \rightarrow \pi\Sigma}^{I=1}|^2 \quad (4.7)$$

$$f_{int}(m_{\pi\Sigma}) = 2\text{Re}(C_{K^-N \rightarrow \bar{K}N}^0 C_{K^-N \rightarrow \bar{K}N}^1 T_{\bar{K}N \rightarrow \pi\Sigma}^{I=0} T_{\bar{K}N \rightarrow \pi\Sigma}^{I=1}) \quad (4.8)$$

Eq.(4.4, 4.5) can be expressed as

$$\begin{aligned} \frac{d\sigma}{d\Omega dM}(\pi^\mp \Sigma^\pm) &= A_{I=0} f_{I=0}(m_{\pi\Sigma}) + A_{I=1} f_{I=1}(m_{\pi\Sigma}) \\ &\quad + \sqrt{A_{I=0} A_{I=1}} f_{int}(m_{\pi\Sigma}) \end{aligned} \quad (4.9)$$

$$\frac{d\sigma}{d\Omega dM}(\pi^- \Sigma^0) = A_{I=1} f_{I=1}(m_{\pi\Sigma}) \quad (4.10)$$

The results of fitting our spectra by varying the model.A by parameterization according to Eq.(4.9-4.10) are shown in Fig.4.19. where $A_{I=0}$ is 0.562 ± 0.015 and $A_{I=1}$ is 1.070 ± 0.040 . $I = 0$ suppresses the overall strength due to the long tail below the $\bar{K}N$ threshold, but still does not

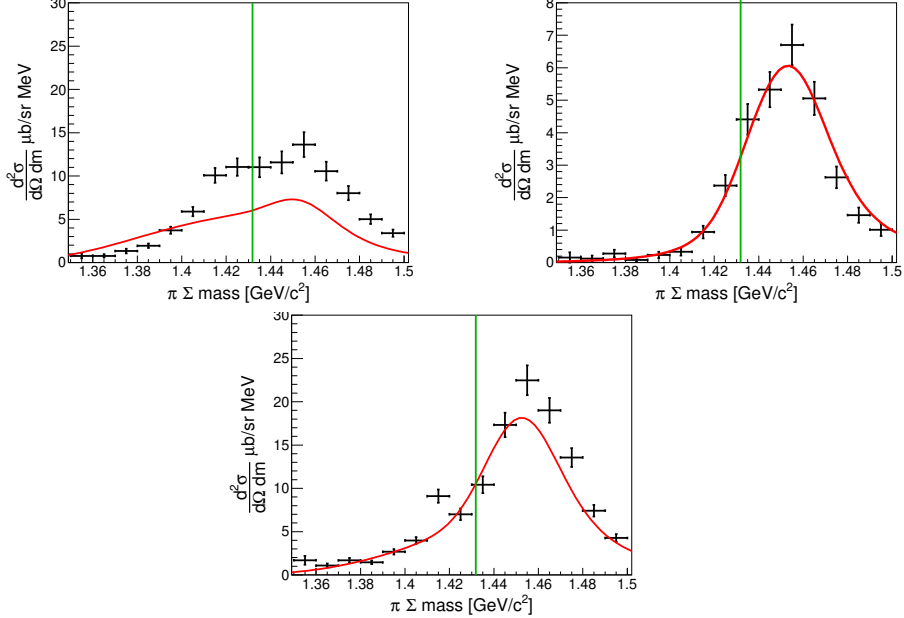


Figure 4.19: These figures show the fitting of parametric strengths of $I = 0$ and $I = 1$ using Model.A. The notation is the same as in Fig.4.18. Only the red line representing Model.A (red line) is plotted.

explain the overall spectral shape. The strength at $I = 1$ remains almost unchanged, while the strength at $I = 0$ is suppressed by the long tail below the $\bar{K}N$ threshold. Therefore, the strength of the interference term is also smaller and deviates from the experimental value. The χ^2/NDF for this fit is $691/42 = 16.4$.

The results of the fit using Model.B are shown in Figure.4.20. The parameters in this fit are $A_{I=0} = 0.721 \pm 0.016$ and $A_{I=1} = 1.423 \pm 0.055$. And, the χ^2/NDF of this fit is $220/42 = 5.25$, which explains our spectra better than the model.A. In this fit, the theoretical value of $I = 1$ is stronger and the strength of $I = 0$ is weaker. Since each value is constrained by the interference term, each spectrum appears to be inadequate in the region above the $\bar{K}N$ threshold. Therefore, we introduce a parameter, A_{int} , which allows us to move the interference term independently, as follows.

$$\begin{aligned} \frac{d\sigma}{d\Omega dm}(\pi^\mp\Sigma^\pm) &= A_{I=0}f_{I=0}(m_{\pi\Sigma}) + A_{I=1}f_{I=1}(m_{\pi\Sigma}) \\ &\quad + \sqrt{A_{I=0}A_{I=1}}A_{int}f_{int}(m_{\pi\Sigma}) \end{aligned} \quad (4.11)$$

$$\frac{d\sigma}{d\Omega dm}(\pi^-\Sigma^0) = A_{I=1}f_{I=1}(m_{\pi\Sigma}) \quad (4.12)$$

We first consider physical mean of the A_{int} parameter. The interference terms are expressed as in Eq(4.13). The phase difference between the

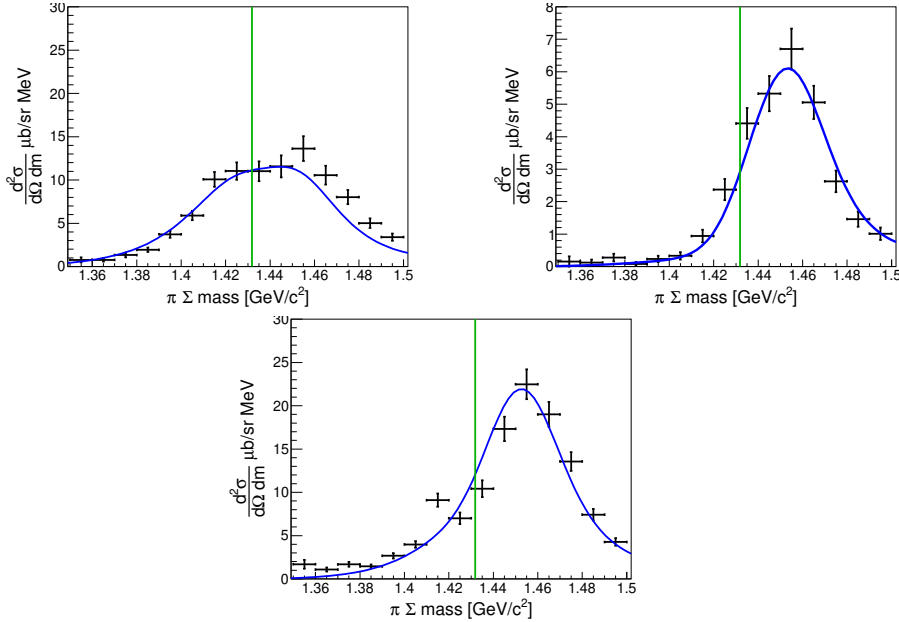


Figure 4.20: These figures show the fitting of parametric strengths of $I = 0$ and $I = 1$ using Model.B. The notation is the same as in Fig.4.18. Only the red line representing Model.B (blue line) is plotted.

terms for each isospin, $C_{K^-N \rightarrow \bar{K}N}^{I=0,1} T_{\bar{K}N \rightarrow \pi\Sigma}^{I=0,1}$ write $\delta\theta$ and the equation can be rewrite as follow.

$$f_{int}(m_{\pi\Sigma}) = 2 |C_{K^-N \rightarrow \bar{K}N}^0 C_{K^-N \rightarrow \bar{K}N}^1 T_{\bar{K}N \rightarrow \pi\Sigma}^{I=0} T_{\bar{K}N \rightarrow \pi\Sigma}^{I=1}| \cos \delta\theta \quad (4.13)$$

In general, the phase of the scattering amplitude depends on the total energy, but in the first step of $K^-p \rightarrow \bar{K}N$ scattering, the total energy is determined by the K^- beam and is independent of the $\pi\Sigma$ mass, which is considered reasonable. Moving the interference terms independently is equivalent to adding to this phase difference a constant parameter independent of the $\pi\Sigma$ mass.

This parameter, which moves the interference terms independently, only affects the $\pi^-\Sigma^+$ and $\pi^+\Sigma^-$ modes, while the $\pi^-\Sigma^0$ mode is determined only by the $I = 1$ strength. Therefore, we obtained the strength of $I = 1$ from the $\pi^-\Sigma^0$ spectrum in the first step and the strength of $I = 0$ and the parameter about the interference term by the fitting of the $\pi^-\Sigma^+$ and the $\pi^+\Sigma^-$ spectra in the next step. As a result, the spectra is obtained as shown in Fig.4.21 and each parameter is obtained as $A_{I=0} = 0.686 \pm 0.017$, $A_{I=1} = 1.462 \pm 0.059$, and $A_{int} = 0.828 \pm 0.030$. Evaluating this fitting with equal weights for all spectra as before the introduction of the interference term gives χ^2/NDF as $187/41 = 4.56$, which is an improvement over before the interference term is introduced.

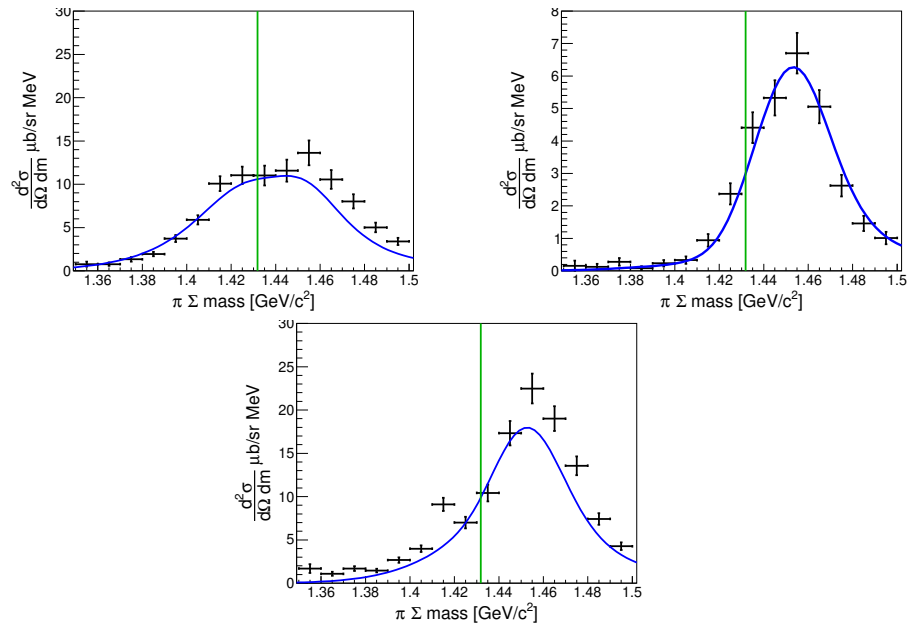


Figure 4.21: This figure shows the results of the fitting using Model.B with the introduction of parameters related to the interference term. The notation is the same as in Fig.4.20. In this fitting, the $I = 1$ strength is determined only from the $\pi^- \Sigma^0$ spectrum, while the other two parameters are determined from the $\pi^- \Sigma^+$ and $\pi^+ \Sigma^-$ spectra.

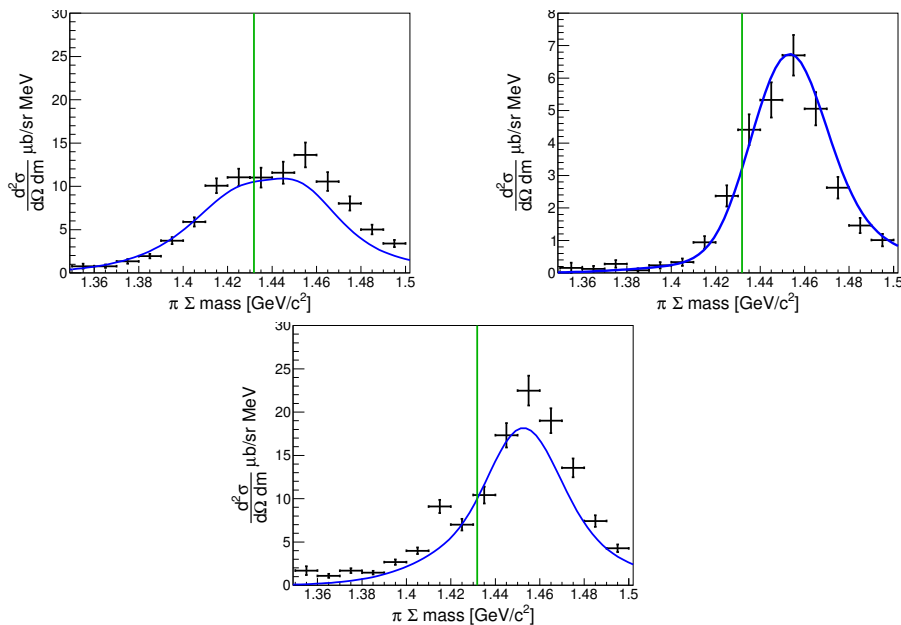


Figure 4.22: This figure shows the results of the fitting using Model.B with the introduction of parameters related to the interference term. The notation is the same as in Fig.4.20. All three parameters are determined simultaneously in this fitting.

We also performed simultaneous fitting of all these parameters in all spectra. The χ^2/NDF of this fit is $184/41 = 4.48$, which is almost the same value as when the strength of $I = 1$ is fixed. As a result, the spectra is obtained as shown in Fig.4.22 and each parameter is obtained as $A_{I=0} = 0.682 \pm 0.017$, $A_{I=1} = 1.570 \pm 0.058$, and $A_{int} = 0.811 \pm 0.030$. The values of these parameters are very close to those of the case with fixed the strength of $I = 1$, and these differences may be considered as systematic errors. Therefore, these parameters are estimated to $A_{I=0} = 0.684 \pm 0.002$ (Systematic) ± 0.017 (fitting), $A_{I=1} = 1.516 \pm 0.054$ (Systematic) $^{+0.058}_{-0.059}$ (fitting), and $A_{int} = 0.820 \pm 0.09$ (Systematic) ± 0.03 (fitting). That implies adding a constant offset of 34.9 ± 0.9 (Systematic) ± 0.3 (fitting) degrees the phase difference between $I = 0$ and $I = 1$.

Chapter 5

Conclusion

We have measured $\pi\Sigma$ masses using the missing mass method with nucleons scattered forward using a K^- beam with $1GeV/c$ and a liquid deuterium target at the K1.8BR beamline in the hadron hall of J-PARC. In this reaction, the irradiated K^- beam kicks out nucleons in deuterium and the decelerated \bar{K} is scattered. By measuring the forward nucleons in particular, the momentum of \bar{K} in the laboratory system is lower, making it more likely to react with residual nucleons. We used CDS to identify the $\pi\Sigma$ final state to $\pi^-\Sigma^+$, $\pi^+\Sigma^-$ and $\pi^0\Sigma^0$ modes.

In this reaction, especially around the $\bar{K}N$ threshold, we can expect S -waves to be enhanced in the second-step $\bar{K}N \rightarrow \pi\Sigma$ scattering due to the smaller angular momentum brought in by the mediating \bar{K} . In fact, no structure is observed in the $\pi^-\Sigma^0$ spectrum at $I = 1$ in the region of the known P -wave, $\Sigma(1385)$. Also in the $\pi^\mp\Sigma^\pm$ spectrum with $I = 0$ and $I = 1$ contributions, no structure is observed neither in $\Sigma(1385)$ nor in the region of $\Lambda(1520)$, known as the D -wave. Therefor, it is confirmed that the S -wave is dominant in present reaction.

It is known that S -wave $\Lambda(1405)$ exists at $I = 0$ just below the KN threshold, and its relation to the $\bar{K}N$ interaction, which is a strong attraction, has long been discussed. Although the elementary process of KN scattering cannot extract information below the KN threshold, this reaction is a 2-step reaction and by reacting the mediating \bar{K} with the residual nucleon, $\bar{K}N \rightarrow \pi\Sigma$ scattering information below the $\bar{K}N$ threshold can be obtained. The $\pi^-\Sigma^0$ spectrum with $I = 1$ has a similar shape to the quasi-elastic scattering from the first-step $K^-N \rightarrow \bar{K}N$ scattering, suggesting that there is no structure in the second-step $\bar{K}N \rightarrow \pi\Sigma$ scattering in this region, while the $\pi^\mp\Sigma^\pm$ spectrum with $I = 0$ shows an excess below $\bar{K}N$ threshold. This means the presence of a $\Lambda(1405)$ contribution. An interference term between $I = 0$ and $I = 1$, which appears as a difference in the $\pi^\mp\Sigma^\pm$ spectra, is also observed.

We decompose the measured spectra into $I = 0$ and $I = 1$ and in-

terference term. Since this experiment was proposed, several theory-based predicted spectra have been calculated. We demonstrate with the respective strength as parameters using the DCC model Model.B which best reproduces our data.

When only the isospin $I = 0$ and $I = 1$ strength are parameterized, it is found that the $I = 0$ strength should be multiplied by a factor of 0.721 ± 0.016 and the $I = 1$ strength by a factor of 1.423 ± 0.055 . The χ^2/NDF of this fit is $220/42 = 5.25$. Furthermore, when the interference term is parameterized to vary independently, we tried two methods: one to determine the intensity of $I = 1$ only from the $\pi^- \Sigma^0$ spectrum, and the other to fit all the parameters at the same time. These fittings of χ^2/NDF are $187/41 = 4.56$ and $184/41 = 4.48$, with values very close and improved compared to before the parameters were introduced. If the difference between these two values is regarded as a systematic error, it was found that the strength of $I = 0$ needs to be multiplied by $A_{I=1} = 1.516 \pm 0.054(\text{Systematic})^{+0.058}_{-0.059}(\text{fitting})$, the strength of $I = 1$ by $A_{int} = 0.820 \pm 0.09(\text{Systematic}) \pm 0.03(\text{fitting})$, and the strength of the interference term by $34.9 \pm 0.9(\text{Systematic}) \pm 0.3(\text{fitting})$. Changing the interference term by this amount corresponds to shifting the phase difference between $I = 0$ and $I = 1$ by $34.9 \pm 0.9(\text{Systematic}) \pm 0.3(\text{fitting})$ degrees. As described, the spectra we obtained contains information on $\bar{K}N \rightarrow \pi\Sigma$ scattering including below the $\bar{K}N$ threshold as second scattering. From that spectra we report experimental values for the $I = 0$ strength as well as the $I = 1$ strength and the phase difference between them.

Appendix A

Appendix Title.1

Appendix B

Appendix Title.2

Bibliography

- [1] R.L. Workman et al. (Particle Data Group), Prog. Theor. Exp. Phys. 2022, 083C01 (2022)
"Review of Particle Physics"
- [2] R. H. Dalitz and S. F. Tuan, Phys. Rev. Lett. 2 (1959).
"Possible Resonant State in Pion-Hyperon Scattering"
- [3] M. H. Alston, L. W. Alvarez, P. Eberhard and M. L. Good,
Phys. Rev. Lett. 6, 698 (1961).
"Study of Resonances of the $\Sigma - \pi$ System"
- [4] R. J. Hemingway, Nucl Phys B **253**, 742 (1985).
"Production of $\Lambda(1405)$ in $K^- p$ Reactions at 4.2GeV/ c "
- [5] R. H. Dalitz and A. Deloff, J. Phys. G17, 281 (1991).
"The Shape and Parameters of the $\Lambda(1405)$ Resonance"
- [6] D. Jido et el., Nucl. Phys. A **725**, 181 (2003).
"Chiral Dynamics of the Two $\Lambda(1405)$ States"
- [7] J. Esmaili, Y. Akaishi, and T. Yamazaki, Phys. Lett. B **686**, 23 (2010)
"Experimental confirmation of the $\Lambda(1405)$ ansatz from resonant formation of a $K^- p$ quasi-bound state in K^- absorption by ${}^3\text{He}$ and ${}^4\text{He}$ "
- [8] M. Niiyama et el., Phys. Rev. C **78**, 035202 (2008).
"Photoproduction of $\Lambda(1405)$ and $\Sigma(1385)$ on the proton at $E_\gamma = 1.5$ - $2.4\text{GeV}/c$ "
- [9] K. Moria for the CLAS Collaboration,
Phys. Rev. C **87**, 035206 (2013).
"Measurement of the $\pi\Sigma$ photoproduction line shapes near the $\Lambda(1405)$ "
- [10] K. Moria for the CLAS Collaboration,
Phys. Rev. Lett. **112**, 082004 (2014).
"Spin and parity measurement of the $\Lambda(1405)$ baryon"

- [11] G. Agakishiev for the HADES Collaboration, Phys. Rev C **87**, 025201 (2013).
"Baryonic Resonances to the $\bar{K}N$ threshold: The case of $\Lambda(1405)$ in pp collisions"
- [12] M. Hassanvand et el., Phys. Rev. C **87**, 055202 (2013)
"Theoretical analysis of $\Lambda(1405) \rightarrow (\pi\Sigma)^0$ mass spectra produced in $p + p \rightarrow p + \Lambda(1405) + p$ reactions"
- [13] B. Conforto et el., Nucl. Phys. B **34**, 41 (1971).
"New experimental results on the Reactions $K^-p \rightarrow \bar{K}N$ and $K^-p \rightarrow \Sigma\pi$ a partial-wave analysis between 430 and 800MeV/ c "
- [14] A. J. Van Horn, Nucl. Phys. B **87**, 145 (1975).
"Energy dependent partial-wave analysis of $K^-p \rightarrow \Lambda\pi^0$ between 1540 and 2215MeV"
- [15] R. J. Hemingway et el., Nucl. Phys. B **91**, 12 (1975).
"New data on $K^-p \rightarrow K^-p$ and K^0n and a partial-wave analysis between 1840 and 2234MeV center of mass energy"
- [16] P. Baillon and P. J. Litchfield, Nucl. Phys. B **94**, 39 (1975).
"Energy-independent partial-wave analysis of $\bar{K}N \rightarrow \Lambda\pi$ between 1540 and 2150 MeV"
- [17] G. P. Gopal et al., Nucl. Phys. B **119**, 362 (1977).
"Partial-wave analyses of KN two-body reactions between 1480 and 2170 MeV"
- [18] H. Zhang et el., Phys. Rev. C **88**, 035204 (2013).
"Partial-wave analysis of $\bar{K}N$ scattering reactions"
- [19] H. Zhang et el., Phys. Rev. C **88**, 035205 (2013).
"Multichannel parametrization of $\bar{K}N$ scattering amplitudes and extraction of resonance parameters"
- [20] H. Kamano et el., Phys. Rev. C **90**, 065202 (2014).
"Dynamical Coupled-Channels Model of K^-p Reactions:
Determination of Partial Wave Amplitudes"
Phys. Rev. C **92**, 025205 (2015).
"Dynamical Coupled-Channels Model of K^-p Reactions. II
Extraction of Λ^* and Σ^* Hyperon Resonances"
Phys. Rev. C **95**, 044903(E) (2015).
- [21] M. Iwasaki et el., Phys. Rev. Lett. **78**, 3067 (1997).
"Observation of Kaonic Hydrogen K_α X Rays"

- [22] G. Beer et el., Phys. Rev. Lett. **94**, 212302 (2005).
"Measurement of the Kaonic Hydrogen X-Ray Spectrum"
- [23] M. Bazzi et el., Phys. Lett. B **704**, 113 (2011).
"A New Measuerment of Kaonic Hydrogen X-Rays"
- [24] Y. Ikeda, T. Hyodo and W. Weise, Phys. Lett. B **706**, 63 (2011)
"Improved constraints on chiral **SU(3)** dynamics from kaonic hydrogen"
- [25] Y. Ikeda, T. Hyodo and W. Weise, Nucl. Phys. A **881**, 98 (2012)
"Chiral **SU(3)** theory of antikaon–nucleon interactions with improved threshold constraints"
- [26] M. Mai and U.-G. Meiβner, Nucl. Phys. A **900**, 51 (2013)
"New insights into antikaon–nucleon scattering and the structure of the $\Lambda(1405)$ "
- [27] Z.-H. Guo and J. Oller, Phys. Rev. C **87**, 3, 035202 (2013),
"Meson-baryon reactions with strangeness -1 within a chiral framework"
- [28] M. Mai and U.-G. Meiβner, Eur. Phys. J. A **51**, 3, 30 (2015),
"Constraints on the chiral unitary $\bar{K}N$ amplitude from $\pi\Sigma K^*$ photo-production data"
- [29] A. Cieplý et al., Nucl. Phys. A 954, 17 (2016),
"On the pole content of coupled channels chiral approaches used for the $\bar{K}N$ system"
- [30] H. Noumi et el., Proposals for the 15th PAC meeting
"Spectroscopic study of hyperon resonances below $\bar{K}N$ threshold via the (K^-, n) reaction on Deuteron"
- [31] O. Braun et el., Nucl. Phys. B **129**, 1 (1977).
"New Information About the Kaon-Nucleon-Hyperon Coupling Constants $g(KN\Sigma(1197))$, $g(KN\Sigma(1385))$ and $g(KN\Lambda(1405))$ "
- [32] D. Jido, E. Oset and T. Sekihara, Eur. Phys. J. A **42**, 257 (2009).
"Kaonic Production of $\Lambda(1405)$ off deuteron target in chiral dynamics"
- [33] J. Yamagata-Sekihara, T. Sekihara, and D. Jido, Prog. Theor. Exp. Phys. **2013**, 043D02 (2013).
"Production of hyperon resonances induced by kaons on a deuteron target"
- [34] S. Ohnishi et el, Phys. Rev. C **93**, 025207 (2016).
"Strcture of the $\Lambda(1405)$ and the $K^-d \rightarrow \pi\Sigma n$ reaction"

- [35] A. Cieplý and J. Smejkal, Nucl. Phys. A **881**, 115 (2012).
"Chirally motivated $\bar{K}N$ amplitudes for in-medium applications"
- [36] E. Oset, A. Ramos, and C. Bennhold, Phys. Lett. B **527**, 99 (2002);
530, 260(E) (2002).
"Low lying $S = -1$ excited baryons and chiral symmetry"
- [37] H. Kamano et al., Phys. Rev. C **94**, 065205 (2016).
"Toward Establishing Low-Lying Λ and Σ Hyperon Resonances with
the $\bar{K} + d \rightarrow \pi + Y + N$ Reaction"
- [38] J. Siebenson and L. Fabbietti, Phys. Rev. C **88**, 055201 (2013)
"Investigation of the $\Lambda(1405)$ line shape observed in pp collisions"
- [39] A. D. Martin, Nucl. Phys. B **179**, 33 (1981).
"Kaon-Nucleon Parameters"
- [40] J. D. Davies et al., Phys. Lett. B **83**, 55 (1979).
"Observation of Kaonic Hydrogen Atom X-rays"
- [41] M. Izuchi et al., Z. Phys. A **297**, 11 (1980).
"Results of the Search for K-series X-rays from Kaonic Hydrogen"
- [42] P. M. Bird et al., Nucl. Phys. A **404**, 482 (1983).
"Kaonic Hydrogen Atom X-rays"
- [43] Y. Ikeda, T. Hyodo, and W. Weise, Nucl. Phys. A **881**, 98 (2012)
"Chiral SU(3) theory of antikaon–nucleon interactions with improved
threshold constraints"
- [44] T. Hashimoto et al., Phys. Rev. Lett. **128**, 112503 (2022).
"Measurements of Strong-Interaction Effects in Kaonic-Helium Isotopes
at Sub-eV Precision with X-Ray Microcalorimeters"
- [45] J. Zmeskal et al., J-PARC P57 Proposal
"Measurement of the Strong Interaction Induced Shift and Width of
the 1s State of Kaonic Deuterium at J-PARC"
- [46] Jonathan M. M. Hall et al., Phys. Rev. Lett. **114**, 132002 (2016).
"Lattice QCD Evidence that the $\Lambda(1405)$ Resonance is an Antikaon-
Nucleon Molecule"
- [47] B. Riley et al., Phys. Rev. D **11**, 3065 (1975)
"Study of $\Sigma^\pm\pi^\mp$ production from negative kaons stopped in 4He "
- [48] M. Niiyama et al., Phys. Rev. C **78**, 035202 (2008).
"Photoproduction of $\Lambda(1405)$ and $\Sigma(1385)$ on the proton at $E_\gamma = 1.5$ -
 $2.4\text{GeV}/c$ "

- J. K. Ahn, Nucl. Phys. A **721**, 715c (2002).
 "Λ(1405) photoproduction at Spring-8/LEPS"
- [49] J.C.Nacher et el., Phys. Lett. B **455**, 55 (1999).
 "Photoproduction of the Λ(1405) on the proton and nuclei"
- [50] L.Fabietti et el., Nucl. Phys. A **914**, 60 (2013).
- [51] K. Miyagawa, J. Haidenbauer, and H. Kamada Phys. Rev. C **97**, 055209 (2018)
 "Faddev approach to the reaction $K - d \rightarrow \pi\Sigma n$ at $p_K = 1.0 GeV/c$ "
- [52] S. Kawasaki et al., JPS Conf. Proc. **13**, 020018 (2017).
 "Spectroscopic Experiment of Λ(1405) via the In-flight $d(K^-, n)n$ Reaction at J-PARC K1BR.8"
- [53] T. Hyodo and D. Jido, Prog. Part. Nucl. Phys. **67**, 55 (2012).
 "The Nature of the Λ(1405) Resonace in Chiral Dynamics"
- [54] K. Agari et el, Prog. Theor. Exp. Phys., 02B009 (2012)
- [55] K. Agari et el, Prog. Theor. Exp. Phys., 02B011 (2012)
- [56] TRANSPORT <http://linac96.web.cern.ch/Linac96/Proceedings/Thursday/THP72/Paper.pdf>
- [57] T. K. Ohska et al., Nuclear Science, IEEE Transactions on **33**, 98 (1986).
- [58] M. Shiozawa and et el., A new TKO system manager board for a dead-time-free data acquisition system, in 1994 IEEE Nuclear Science Symposium-NSS'94, pages 632–635, (1994)
- [59] M. Iio et al., Nucl. Instrum. Methods Phys. Res., Sect. **A** **687**, 1 (2012).
- [60] S. Agostinelli et al., Nucl. Instrum. Methods Phys. Res., Sect. **A** **506**, 250 (2003)
 J. Allison et el., IEEE Transactions on Phys. Sci. **53**, 207 (2006)
 J.Allison et al., Nucl. Instrum. Methods Phys. Res., Sect. **A** **835**, 186 (2016)
- [61] K. Fuji, https://www-jlc.kek.jp/subg/offl/lib/docs/helix_manip/node3.html (1968).
- [62] Opera Electromagnetic FEA Solution Software
- [63] V. Flaminio et al., CERN-HARA-87-01, 121 (1983).
- [64] M.Jones et el, Nucl. Phys. B **90**, 349 (1975)
- [65] R. Barlow and C. Beeston, Comp. Phys. Comm. **77**, 219 (1993).
 "Fitting using finite Monte Carlo samples"

- [66] A. Nappi, Comp. Phys. Comm. **180**, 269 (2009).
- [67] C.J.S. Damerell et. el., Nucl. Phys. B**129**, 397 (1977). ”
 K^-n elastic scattering between 610 and 840 MeV/ c ”
- [68] M. Jones, R. Levi, Setti, D. Merrill and R. D. Tripp, Phys. Rev. B**90**, 349 (1975).
- [69] M. Bernheim and et. el., Nucl. Phys. A**365**, 349, (1981).
- [70] R. Machleidt, Phys. Rev. C**63**, 024001 (2001).
- [71] R. Barlow and C. Beeston, Comp. Phys. Comm. **77**, 219 (1993).
- [72] S. Agostinelli et al., Nuclear Instruments and Methods in Physics Research Section A: Accelerators, Spectrometers, Detectors and Associated Equipment **506**, 250 (2003).
J.Allison et el., Nuclear Instruments and Methods in Physics Research Section A: Accelerators, Spectrometers, Detectors and Associated Equipment **835**, 186 (2016).